

Distortion of a Harmonic Elastic Wave Reflected From a Dry Friction Support

M. J. Leamy

Graduate Student Research Assistant

J. R. Barber

Professor,
Mem. ASME

N. C. Perkins

Associate Professor,
Mem. ASME

Department of Mechanical Engineering
and Applied Mechanics,
The University of Michigan,
2250 G. G. Brown,
Ann Arbor, MI 48109-2125

This study is motivated by the need to understand the elastodynamic response of belts in frictional contact with pulleys. To this end, a simplified model for belt/pulley contact is used to investigate the dynamic response of a belt subject to a train of harmonic tension waves. Through a nondimensionalization, a single dimensionless parameter Ω is identified which governs the dynamic response. A numerical solution is developed and exercised over a wide range of values of Ω . An approximate closed-form solution is derived assuming the belt stretches quasi-statically, and is shown to yield accurate results for small values of Ω . Reported results include the distortion of an initially harmonic tension wave, the energy reflected from the frictional support, and the distance harmonic waves penetrate into the support. The results suggest that the quasi-static stretching assumption may be further utilized as a modeling simplification for belt drives characterized by values of $\Omega < \frac{1}{3}$.

1 Introduction

This study is principally motivated by belt drive mechanics which have been studied by many researchers, starting with Leonard Euler (1762). Euler proposed the well-known *capstan* formula for the tension distribution in a belt wrapped around a fixed pulley or a capstan (a fixed post used in docking a ship). A comprehensive survey of belt drive mechanics after Euler and up to 1981 is provided by Fawcett (1981). Much of the research cited in Fawcett (1981) and work since its appearance has been concerned with either (1) frictional contact (slip) between a belt and a steadily rotating pulley (neglecting vibratory effects) or (2) vibration of belts neglecting frictional contact.

Early research on frictional contact was carried out by Grashof (1883), who studied frictional mechanics of belt drives under steady operating speeds and applied torques. The belt was treated as a string and the mechanism of elastic creep of the belt along the pulley was shown to yield a single *slip arc* on the exit region of the pulley. In this classical creep theory, the transition from low to high tension (or vice-versa) occurs in this slip arc; see also (Johnson, 1985). Later investigators, including Firkbank (1970) and Gerbert (1991, 1996), considered the influence of belt thickness as well as its length, and proposed revised estimates of the extent of the slip zone based on belt creep, shear, radial deformation, and seating/unseating behavior. These new analyses predicted tension transitions in the *adhesion* arc as well as in the slip arc. Finally, Townsend and Salisbury (1988) used a control volume approach to calculate the energy efficiency of a two-pulley belt drive based solely on the stiffness per unit length of the belt and the transmitted torque. Again, the operating conditions of the drive were assumed to be steady.

More recently, substantial research has concentrated on serpentine belt drive systems which include an automatic tensioning element, as commonly employed in vehicle front end

accessory drives. These investigations, including Barker et al. (1991), Hwang et al. (1994), Beikmann et al. (1996), Kraver et al. (1996), and Leamy and Perkins (1997), have focused on the dynamic response of the belt and the accessory pulleys due to crankshaft excitation. Predictions of transverse and/or longitudinal belt vibration and pulley rotational response employed idealized models of the belt/pulley contact. For instance, in Barker et al. (1991), Hwang et al. (1994), Kraver et al. (1996), and Leamy and Perkins (1997), the belt/pulley contact was modeled by a linear spring representing an equivalent length of belt in an assumed slip arc.

The vibration of the belt spans and pulleys generates tension waves in the belt which influence the belt/pulley contact in a manner yet to be understood. For instance, the amplitude and frequency of these tension fluctuations may influence the number and location of slip arcs at the interface, which in turn may affect the vibrational response. The resulting coupled problem of vibrational response and frictional contact has yet to be investigated.

In this paper, we consider a simplified model of the belt and the belt/pulley interface as a starting point for understanding the coupled response. The model, illustrated in Fig. 1, consists of a length of belt resting partly on a frictional interface. A Coulomb law representation of the dry friction is chosen for its simplicity and ability to capture stick-slip motions, although other friction laws are worthy of future studies (see, for example, Tabor (1981) and Oden and Martins (1985)). In this study, we consider incoming *harmonic* tension waves that impinge upon the support and are reflected back with distorted shape. Quantifying this distortion, the reflected wave energy, and the distance the waves penetrate into the support, are objectives of this study. To this end, a numerical solution method and an approximate closed-form solution are proposed, both of which generalize easily to varied friction laws.

Similar models are also employed to evaluate the response of driven piles (E. Smith, 1960; I. Smith, 1988). Nikitin and Tyurekhodgaev (1990) analyze a semi-infinite rod, resting on a Coulomb surface and subject to various end conditions, using the method of characteristics. Exact solutions for wave propagation are obtained for cases when a constant stress or velocity is applied to the rod's end, or when the end is impacted by a rigid body. These studies, which focus on wave propagation in elastic continuum with friction, also relate to broader topics concerning friction-induced vibration (see, for example, Popp

Contributed by the Applied Mechanics Division of THE AMERICAN SOCIETY OF MECHANICAL ENGINEERS for publication in the ASME JOURNAL OF APPLIED MECHANICS.

Discussion on the paper should be addressed to the Technical Editor, Professor Lewis T. Wheeler, Department of Mechanical Engineering, University of Houston, Houston, TX 77204-4792, and will be accepted until four months after final publication of the paper itself in the ASME JOURNAL OF APPLIED MECHANICS.

Manuscript received by the ASME Applied Mechanics Division, Jan. 6, 1998; final revision, June 16, 1998. Associate Technical Editor: L. T. Wheeler.

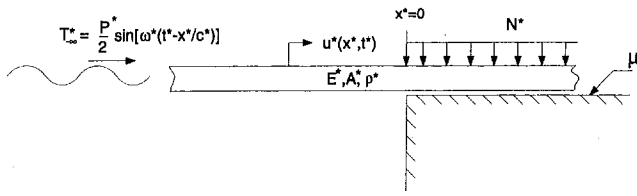


Fig. 1 System model

and Stelter (1990) and the review provided in Ibrahim (1994a, b)).

2 System Model

The displacement $u^*(x^*, t^*)$ of the infinite rod shown in Fig. 1 is governed by the *nonlinear* wave equation,

$$\frac{\partial^2 u^*}{\partial x^{*2}} - \frac{\rho^* A^*}{E^* A^*} \frac{\partial^2 u^*}{\partial t^{*2}} - \frac{\mu N^*}{E^* A^*} \operatorname{sgn} \left(\frac{\partial u^*}{\partial t^*} \right) H(x^*) = 0, \quad (1)$$

on the infinite domain $(-\infty < x^* < +\infty)$, where E^* , ρ^* , and A^* represent the Young's modulus, volume density, and cross-sectional area, respectively, of the rod. The coefficient of friction, μ , describes the Coulomb surface supporting the rod in the region $x^* \geq 0$ where N^* denotes the normal force per unit length. In (1), sgn denotes the *signum* operator while $H(x^*)$ is the Heaviside step function. The rod is subject to a steady train of harmonic tension waves of amplitude $P^*/2$ radiating to the right from $x^* = -\infty$ and defined by

$$T_{-\infty}^* = \frac{P^*}{2} \sin \left[\omega^* \left(t^* - \frac{x^*}{c^*} \right) \right] \quad (2)$$

where

$$T^*(x^*, t^*) = E^* A^* \frac{\partial u^*}{\partial x^*} \quad (3)$$

is the tension in the belt, ω^* is the excitation frequency, and $c^* = \sqrt{E^*/\rho^*}$ is the longitudinal wave speed.

Introducing the dimensionless quantities,

$$u = \frac{\mu N^* E^* A^*}{P^{*2}} u^*, \quad x = \frac{\mu N^*}{P^*} x^*, \quad t = \frac{\mu N^* c^*}{P^*} t^*, \quad (4)$$

reduces (1)–(3) to

$$\frac{\partial^2 u}{\partial x^2} - \frac{\partial^2 u}{\partial t^2} - \operatorname{sgn} \left(\frac{\partial u}{\partial t} \right) H(x) = 0 \quad (5)$$

$$T_{-\infty} = \frac{1}{2} \sin [\Omega(t - x)] \quad (6)$$

$$T(x, t) \equiv \frac{T^*}{P^*} = \frac{\partial u}{\partial x} \quad (7)$$

where

$$\Omega = \frac{\omega^* P^*}{\mu N^* c^*}. \quad (8)$$

The dimensionless Eqs. (5)–(7) reveal that the single parameter Ω classifies all problems of the type shown in Fig. 1.

3 Numerical Solution

We first develop a numerical solution for the elastodynamic model of Fig. 1. This requires that the semi-infinite rod of Fig. 1 be replaced by a finite rod, as shown in Fig. 2. Employing a lumped parameter representation and using the dimensionless

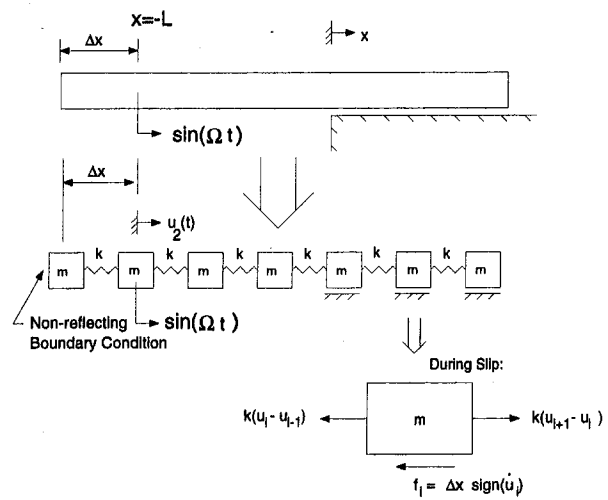


Fig. 2 Lumped parameter model

quantities in (4), the elastic rod is discretized into discrete springs and masses with element (dimensionless) stiffness and mass

$$k = \frac{1}{\Delta x}, \quad m = \Delta x,$$

respectively, where Δx is the discretization length. In Fig. 2, $u_i(t)$ denotes the dimensionless position of the i th element.

Simulation of the radiation condition at $x = -\infty$ of Fig. 1 is accomplished as follows. First, an applied load ($\sin(\Omega t)$) on the second mass yields rightward and leftward moving tension waves of amplitude $\frac{1}{2}$. The rightward wave simulates the desired radiation from $x = -\infty$. The total leftward moving tension waves, including tension wave components from the loading on the second mass and any reflected wave from the frictional

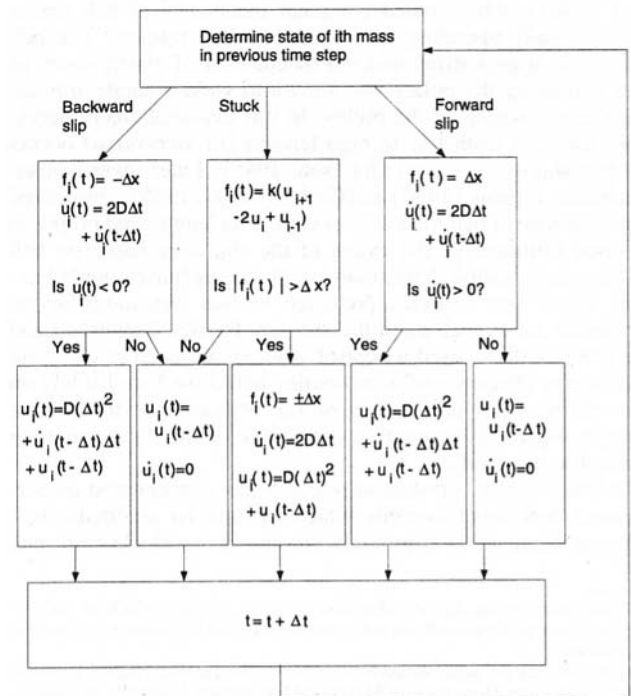


Fig. 3 Flow of calculations in numerical solution for elements in the support region, $x > 0$. The quantity $D = \{k[u_{i-1}(t - \Delta t) - 2u_i(t - \Delta t) + u_{i+1}(t - \Delta t)]/(2m)$.

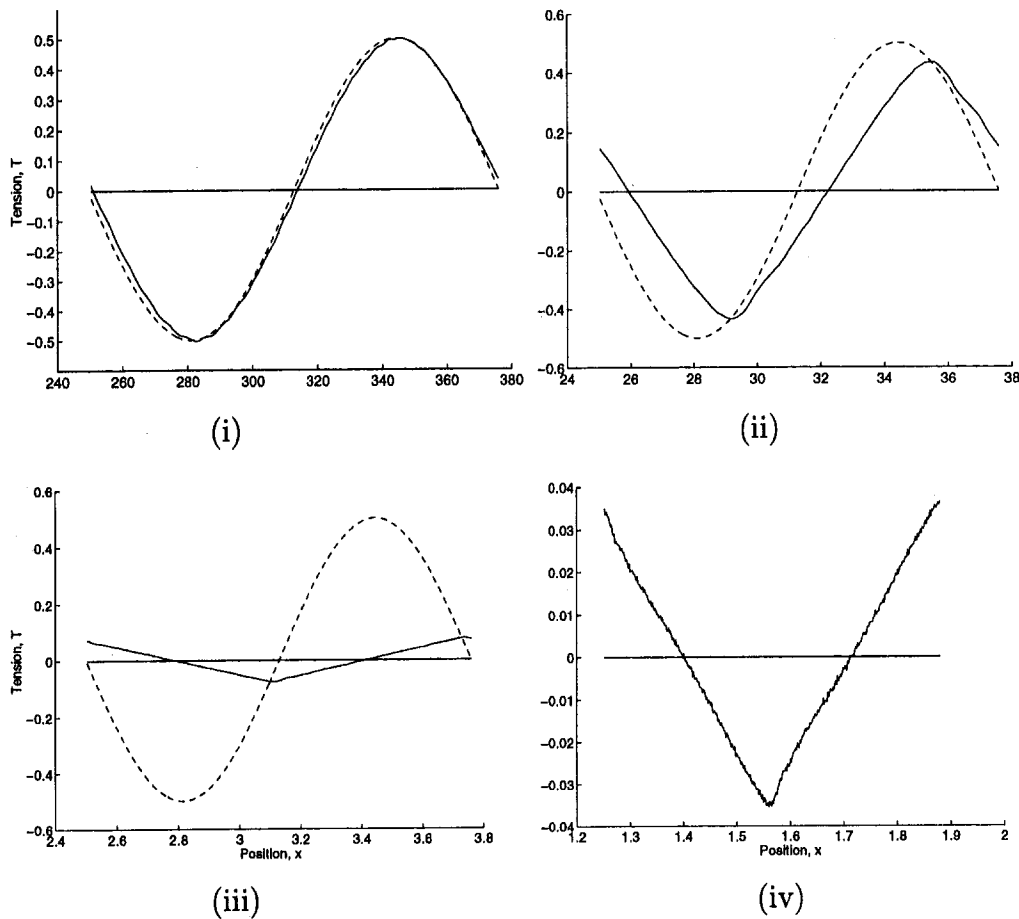


Fig. 4 Steady-state reflected tension waveforms at four values of Ω . Solid curves denote the numerical solution for a frictional support and dashed curves denote the solution for a fixed end. (i) $\Omega = 0.05$; (ii) $\Omega = 0.5$; (iii) $\Omega = 5.0$; (iv) $\Omega = 10.0$.

support, are then absorbed by a nonreflecting boundary condition (Givoli, 1991) at the site of the first element. This boundary condition, given by

$$\left. \frac{\partial u}{\partial x} \right|_{x=-L-\Delta x} = \left. \frac{\partial u}{\partial t} \right|_{x=-L-\Delta x}, \quad (9)$$

leads to a finite difference approximation,

$$\frac{u_2(t - \Delta t) - u_1(t - \Delta t)}{\Delta x} = \frac{u_1(t) - u_1(t - \Delta t)}{\Delta t}, \quad (10)$$

where the spatial derivative has been approximated in a forward (+x) sense (to anticipate the leftward moving wave) and the time derivative is evaluated using u_1 . Solving (10) for $u_1(t)$,

$$u_1(t) = \frac{\Delta t}{\Delta x} u_2(t - \Delta t) + \left(1 - \frac{\Delta t}{\Delta x}\right) u_1(t - \Delta t) \quad (11)$$

provides the position of the first element at each time step in the subsequent numerical simulations.

The equation of motion for every other element ($i = 2, 3, 4, \dots$) is used to simulate the response of the remainder of the rod. Figure 3 provides a flow diagram of the algorithm used to advance the simulation. This figure describes one time-step advancement of the i th element in the support region, $x > 0$, with a simpler algorithm for each element in the unsupported region, $x < 0$. The algorithm begins with calculating the frictional force (f_i) on the element based on the direction of slip at the end of the previous time step. If the element was stuck

in the previous time step, the friction force is calculated to be that which is required to maintain equilibrium, and the element is allowed to move only if the magnitude of this force exceeds the maximum frictional force, Δx . If the element was sliding at the end of the previous step, then f_i is set equal to $\pm \Delta x$ and motion is arrested when the element's velocity changes sign. Acceleration, velocity, and position calculations follow from the equations of motion, as detailed in Fig. 3.

An appropriate time-step and spatial discretization is chosen such that the numerical solutions which follow are fully converged with 125 elements per wavelength used in the unsupported region, and at least 130 elements used over the distance that the tension waves penetrate into the support. At small Ω , the penetration distance is much smaller than a wavelength, and this length scale ultimately determines the discretization length.

3.1 Results of Numerical Simulation. The numerical solution is used to investigate what happens to a harmonic disturbance which propagates into a frictional support. In particular, attention focuses on the amplitude and shape of the tension wave which is subsequently reflected from the support.

Figure 4 shows the form of the steady-state reflected tension wave for four sample values of Ω spanning three orders of magnitude. In the first three cases, the waveform reflected from a fixed end (perfect reflection) is also shown for comparison. At small values of Ω , the waveform is nearly harmonic and nearly in phase with the wave reflected from a fixed end. As Ω increases, however, the phase is shifted as the wave penetrates further into the frictional support, and the reflected wave becomes distorted, ultimately conforming to the limiting shape of a nearly triangular

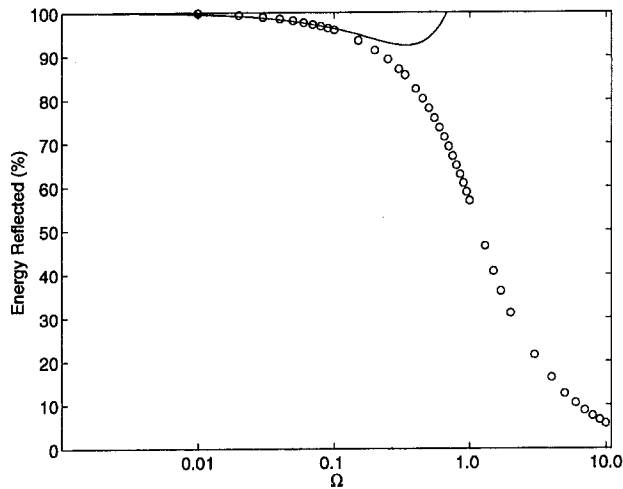


Fig. 5 Percent energy reflected versus Ω for the quasi-static solution (—) and the numerical solution (○)

wave at large Ω . As a result of the increased penetration distance (and associated energy loss), the amplitude of the reflected wave decreases monotonically with increasing Ω .

The loss of energy due to frictional dissipation is apparent in Fig. 5, which shows the energy of the reflected wave as a function of Ω . Less than five percent of the incoming energy is reflected for values of Ω exceeding 10.

The gradual distortion of the harmonic wave with Ω is further evaluated by examining the Fourier content of the reflected wave form. Figure 6 illustrates the magnitude of the first three nonzero Fourier coefficients (first, third, and fifth harmonics) of the reflected wave form, as well as the phase of the first harmonic, as functions of Ω . This phase defines a lag between the first harmonic of the reflected wave and the reference wave reflected from a fixed end. The Fourier coefficients associated with the numerical solution are obtained by numerical quadrature. For small values of Ω in Fig. 6, the wave reflected from the frictional support deviates little in either amplitude or phase from the pure harmonic reflected from the fixed end. As Ω increases, the amplitude of the reflected wave decreases, and the relative contributions of the higher harmonics increase. As the value of Ω increases still further, the higher harmonics achieve a maximum magnitude (near $\Omega = 1$) and then decay with increasing Ω . The phase lag of the first harmonic approaches the limiting value of $\pi/2$. As Ω approaches infinity, all coefficients approach zero and the frictional support acts as an anechoic termination.

Consider next the steady-state tension developed in the support region. Figure 7 illustrates the envelope of the tension wave that penetrates into the support region. The envelope is generated by noting the maximum and minimum tension of each element as a train of tension waves impinge upon the support region. In particular, an average envelope is calculated from the envelopes produced by initially compressive loading ($+\sin \Omega t$) and initially tensile loading ($-\sin \Omega t$). For small Ω , the support creates near perfect reflections and the magnitude of the tension at the entrance to the frictional support is nearly twice the amplitude of the incoming wave, as shown in Fig. 7. As Ω increases, the penetration distance (dimensionless) stretches slightly and the magnitude of the tension envelope at the entrance approaches $\pm \frac{1}{2}$ as the waves pass through with little reflection.

4 Limiting Cases

Two limiting regimes are identified based on limiting values of Ω : (1) a regime for small Ω wherein the rod responds quasi-

statically and (2) a regime for large Ω wherein the frictional support approaches an anechoic termination. These limits are discussed next.

4.1 Quasi-Static Regime (Small Ω). Consider again the rod of Fig. 2 subject to the applied load $\sin \Omega t$ near the limit $\Omega \rightarrow 0$. This limit may be realized as the excitation frequency $\omega^* \rightarrow 0$ or as the wave speed $c^* \rightarrow \infty$, or as the excitation wavelength $\lambda^* = 2\pi c^*/\omega^*$ approaches infinity. In all cases the rod responds in a quasi-static manner and the inertia term in (5) is negligibly small. The quasi-static tension distribution may then be evaluated from a free-body diagram of the rod. The displacement $u(x, t)$ follows upon integrating the constitutive law ($\partial u/\partial x = T$).

Figure 8 illustrates the resulting tension distribution for the half cycle during which the load decreases. The shaded trough develops from the fully loaded tension distribution (denoted by the dashed line) as the tension applied to the end of the rod decreases. As this load decreases, a slip zone of opposite slip direction (as compared to the fully loaded slip direction) begins at $x = 0$ and grows towards increasing x , eventually occupying the entire penetration distance when $\sin(\Omega t) = -1$. Note that since the displacement at $x = 1$ is zero, the displacement at $x = -L$ is simply proportional to the shaded area in Fig. 8, namely

$$u(-L, t) = [L + \frac{1}{2}] \sin(\Omega t) - \frac{1}{4} \sin^2(\Omega t) + \frac{1}{4},$$

$$\frac{(4m+1)\pi}{2} < \Omega t < \frac{(4m+3)\pi}{2}, \quad (12)$$

where m is an integer. By similar arguments, during the half cycle when the load is increasing,

$$u(-L, t) = [L + \frac{1}{2}] \sin(\Omega t) + \frac{1}{4} \sin^2(\Omega t) - \frac{1}{4},$$

$$\frac{(4m+3)\pi}{2} < \Omega t < \frac{(4m+5)\pi}{2}. \quad (13)$$

The quasi-static stretching assumption provides a solution for the displacement and tension which are spatially uniform in the unsupported region, and parameterized by time. The wave-like behavior is lost, but the time parameterization can still be exploited to yield an approximate waveform by solving an associated elastodynamic problem for the subdomain to the left of the loading.

To this end, consider a semi-infinite bar $-\infty < x < -L$ whose end $x = -L$ is subjected to the displacement $u(-L, t)$ obtained above. The resulting waveform of this elastodynamic problem can then be compared to that obtained from the numerical simulation. This approximate elastodynamic solution follows directly from (12) and (13) upon replacing Ωt with $\phi = \Omega(x + L + t)$ and is valid for $x < -L$:

$$u(x, t) = \begin{cases} [L + \frac{1}{2}] \sin \phi - \frac{1}{4} \sin^2 \phi + \frac{1}{4}, \\ \frac{(4m+1)\pi}{2} < \phi < \frac{(4m+3)\pi}{2} \\ [L + \frac{1}{2}] \sin \phi + \frac{1}{4} \sin^2 \phi - \frac{1}{4}, \\ \frac{(4m+3)\pi}{2} < \phi < \frac{(4m+5)\pi}{2} \end{cases} \quad (14)$$

The associated tension distribution is

$$T(x, t) = \begin{cases} \Omega[L + \frac{1}{2}] \cos \phi - \frac{1}{2} \Omega \sin \phi \cos \phi, \\ \frac{(4m+1)\pi}{2} < \phi < \frac{(4m+3)\pi}{2} \\ \Omega[L + \frac{1}{2}] \cos \phi + \frac{1}{2} \Omega \sin \phi \cos \phi, \\ \frac{(4m+3)\pi}{2} < \phi < \frac{(4m+5)\pi}{2} \end{cases} \quad (15)$$

An approximate solution for the rod subjected to harmonic

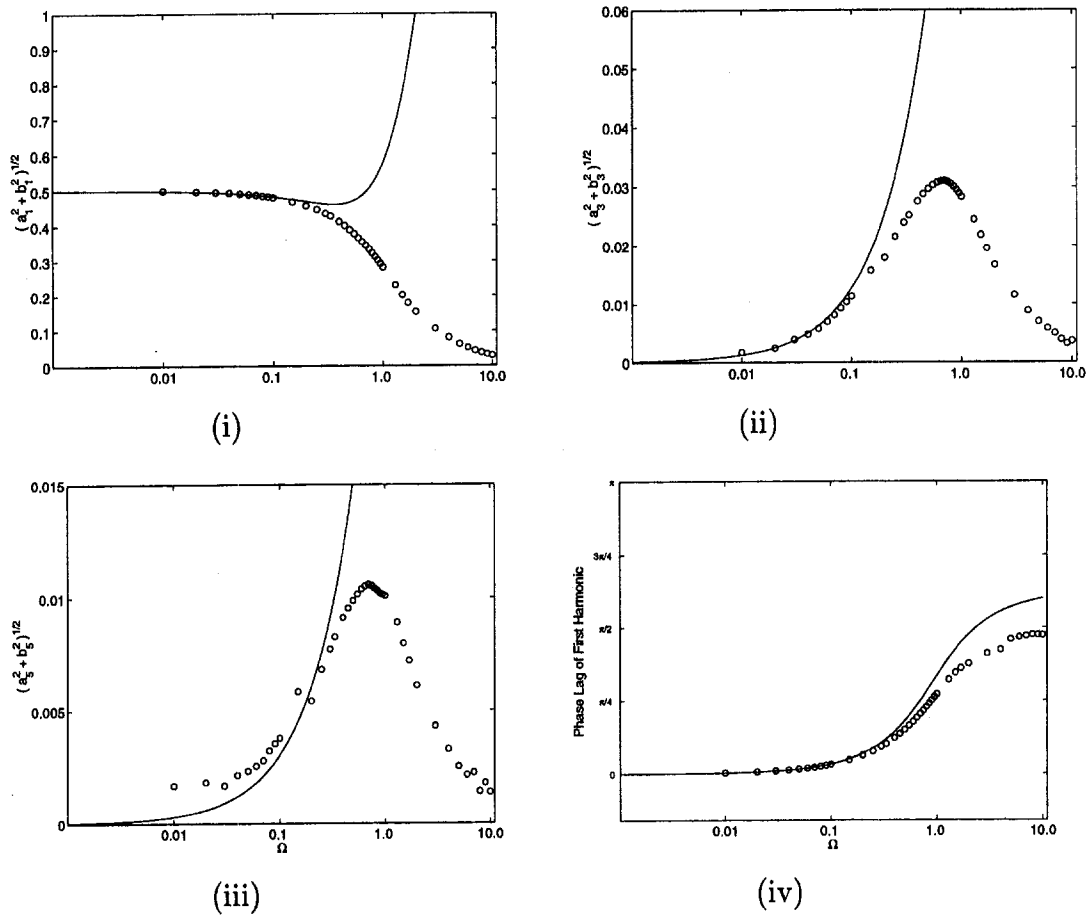


Fig. 6 Fourier coefficients versus Ω . The magnitudes of the first, third, and fifth harmonic are shown in (i)–(iii), respectively, and the phase of the first harmonic is shown in (iv). Numerical solution denoted by \circ ; quasi-static solution denoted by —.

radiation from $x = -\infty$, Fig. 1, can be recovered from (15) by adding the incoming rightward moving tension wave

$$\frac{1}{2} \sin [\Omega(x + L - t)]$$

in $x < -L$ and cancelling the leftward moving tension wave

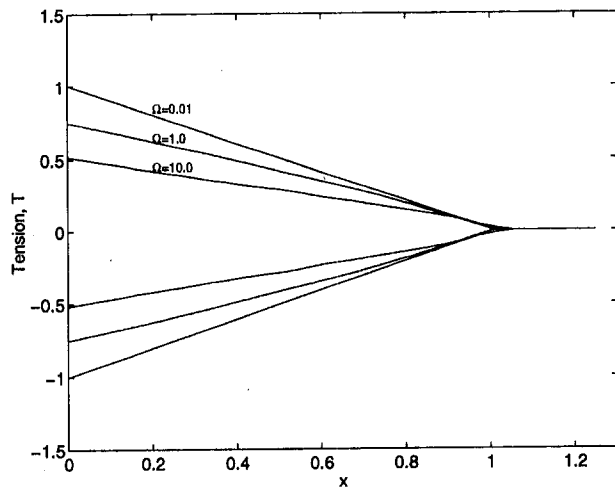


Fig. 7 Envelope of tension distribution in support region. Plotted are envelopes of dimensionless tension (T) versus dimensionless position (x) for $\Omega = 0.01, 1.0$, and 10.0 . The amplitude of the envelope monotonically decreases with increasing Ω .

$$\frac{1}{2} \sin [\Omega(x + L + t)]$$

in $x < -L$. Additionally, the choice of L is arbitrary and selecting $L = 0$, simplifies the expression further. The resulting solution, valid for $x < 0$, is

$$T(x, t) = \begin{cases} T^- = \frac{1}{2}\Omega \cos \phi - \frac{1}{4}\Omega \sin (2\phi) - \frac{1}{2} \sin \phi \\ \quad + \frac{1}{2} \sin \theta, & \frac{(4m+1)\pi}{2} < \phi < \frac{(4m+3)\pi}{2} \\ T^+ = \frac{1}{2}\Omega \cos \phi + \frac{1}{4}\Omega \sin (2\phi) - \frac{1}{2} \sin \phi \\ \quad + \frac{1}{2} \sin \theta, & \frac{(4m+3)\pi}{2} < \phi < \frac{(4m+5)\pi}{2} \end{cases} \quad (16)$$

with now

$$\phi = \Omega(x + t)$$

$$\theta = \Omega(x - t)$$

where the region $x < 0$ now lies in front of the source. Having a solution valid in front of the source makes comparisons to the numerical results more convenient, and is the motivation for this step. The superscripts + and - distinguish the half cycles in which the loading is increasing + (decreasing -).

The accuracy of the quasi-static solution is now assessed. To this end, consider a Fourier series decomposition of (16) as the means to compare the waveform based on quasi-statics to that

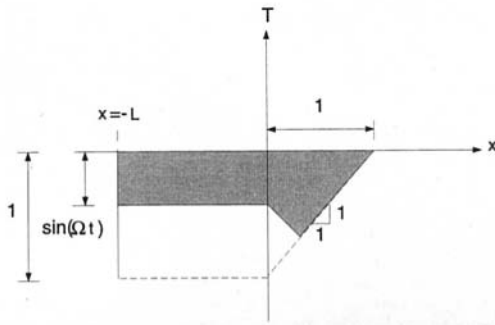


Fig. 8 Quasi-static tension distribution (decreasing excitation force). Dashed line represents the tension distribution for the fully loaded rod.

obtained from the numerical solution. Defining a Fourier series for the tension field,

$$T(x, t) = a_0(t) + \sum_{n=1}^{\infty} [a_n(t) \cos(n\Omega x) + b_n(t) \sin(n\Omega x)], \quad (17)$$

the Fourier coefficients ($a_n(t)$, $b_n(t)$) are evaluated over a single wavelength ($m = 0$ in 16)¹:

$$a_0(t) = \frac{\Omega}{2\pi} \int_{(\pi/2\Omega)-t}^{(3\pi/2\Omega)-t} T^-(x, t) dx + \frac{\Omega}{2\pi} \int_{(3\pi/2\Omega)-t}^{(5\pi/2\Omega)-t} T^+(x, t) dx \quad (18)$$

$$a_n(t) = \frac{\Omega}{\pi} \int_{(\pi/2\Omega)-t}^{(3\pi/2\Omega)-t} T^-(x, t) \cos(n\Omega x) dx + \frac{\Omega}{\pi} \int_{(3\pi/2\Omega)-t}^{(5\pi/2\Omega)-t} T^+(x, t) \cos(n\Omega x) dx \quad (19)$$

$$b_n(t) = \frac{\Omega}{\pi} \int_{(\pi/2\Omega)-t}^{(3\pi/2\Omega)-t} T^-(x, t) \sin(n\Omega x) dx + \frac{\Omega}{\pi} \int_{(3\pi/2\Omega)-t}^{(5\pi/2\Omega)-t} T^+(x, t) \sin(n\Omega x) dx. \quad (20)$$

Evaluation of (18)–(20) reveals that all even integer Fourier coefficients (a_0 , a_2 , \dots , b_2 , b_4 , \dots) vanish, consistent with the fact that the Coulomb law describes an odd distribution (Pierre et al., 1985). The odd-numbered coefficients are

$$a_1 = \left[\frac{2\Omega}{3\pi} - 1 \right] \sin(\Omega t) + \frac{\Omega}{2} \cos(\Omega t) \quad (21)$$

$$b_1 = \frac{2\Omega}{3\pi} \cos(\Omega t) - \frac{\Omega}{2} \sin(\Omega t) \quad (22)$$

$$a_n = (-1)^{(n+1)/2} \frac{2}{n^2 - 4} \frac{\Omega}{\pi} \sin(n\Omega t), \quad n = 3, 5, \dots \quad (23)$$

$$b_n = (-1)^{(n+1)/2} \frac{2}{n^2 - 4} \frac{\Omega}{\pi} \cos(n\Omega t), \quad n = 3, 5, \dots \quad (24)$$

Note that the coefficients for a given order (n) depend solely on the dimensionless parameter Ω , as expected.

Finally, note that the *reflected* component of the tension waveform may be extracted from the Fourier series (17) by subtracting the coefficients due to the incoming tension wave.

¹Note that the coefficients are calculated with integration limits that move with the moving tension regions. Alternatively, the coefficients can be calculated over a *fixed* spatial region corresponding to one excitation wavelength. These approaches yield the same expressions for the coefficients as required.

The resulting Fourier series of the reflected wave component is again (17) with

$$a_1 = \left[\frac{2\Omega}{3\pi} - \frac{1}{2} \right] \sin(\Omega t) + \frac{\Omega}{2} \cos(\Omega t) \quad (25)$$

$$b_1 = \left[\frac{2\Omega}{3\pi} - \frac{1}{2} \right] \cos(\Omega t) - \frac{\Omega}{2} \sin(\Omega t) \quad (26)$$

and a_n and b_n ($n = 3, 5, 7, \dots$) again given by (23) and (24).

4.1.1 Results of Quasi-Static Analysis. The Fourier coefficients of the reflected tension wave for the quasi-static solution are superimposed on those for the full elastodynamic solution in Fig. 6. The coefficients for the quasi-static solution converge to those of the numerical solution as $\Omega \rightarrow 0$. The convergence of the coefficients for the higher ($n > 5$) harmonics is ultimately limited by the discretization size. A trend captured by both the numerical and quasi-static solutions at small Ω is the increasing importance of the super-harmonics as Ω increases from zero, and the decreasing importance of the fundamental harmonic. This trend continues in the numerical solution until $\Omega \cong 1.0$, beyond which all harmonics decay. This decay is not captured by the quasi-static solution which ultimately predicts for larger values of Ω that the reflected wave possesses a greater amplitude (and thus energy) than the originating wave (a physical impossibility) (refer also to Fig. 5).

Observe from Fig. 6 that a regime for Ω exists in which the quasi-static solution accurately predicts the reflected waveform and that this regime can be identified by examining the fundamental harmonic alone. The higher harmonics have a negligible effect on the magnitude and phase of the reflected wave. Values for $\Omega < \frac{1}{3}$ ensure that the quasi-static solution predicts the magnitude of the reflected wave to within eight percent and the phase to within two percent, when compared to the elastodynamic solution. Figure 5 also indicates the fidelity of the quasi-static solution. For $\Omega < \frac{1}{3}$, both solutions predict near identical reflected wave energy.

A final comparison of the numerical and quasi-static solution is provided in Figs. 7 and 8. From Fig. 8, the quasi-static solution predicts a triangular tension envelope in the support region (see the dotted line shown in the Fig.). From Fig. 7 it is observed that the tension envelope from the numerical solution approaches that of the quasi-static solution for small Ω , with no observable difference between envelopes at $\Omega = 0.01$. Further comparisons reveal an interesting observation; namely, the dimensionless penetration distance (S) of the quasi-static solution predicts the penetration with errors less than five percent over the large range of Ω considered in Fig. 7.

4.2 Anechoic Termination Regime (Large Ω). From Figs. 4–6, as Ω increases, the amplitude of the reflected wave decreases, and the reflected wave energy decreases as the waveform converges to a nearly triangular profile. At sufficiently high Ω , such as $\Omega \geq 10$, nearly all the energy (~95 percent) of the incoming waves is absorbed by the support and an anechoic termination is effectively realized. Thus, in systems characterized by a large Ω , the frictional support may be adequately modeled by an anechoic boundary condition in the form of (9).

5 Conclusions

A single dimensionless parameter Ω has been identified which governs the dynamic response of an infinite rod subject to harmonic tension waves and interacting with a dry friction surface. Incoming harmonic tension waves partially reflect from the frictional support and both the degree of reflection and the degree of distortion are controlled solely by Ω . This distortion and energy reflection have been quantified as a function of Ω using an approximate closed-form quasi-static solution and a

numerical solution. The results of this study suggest that a quasi-static model for belt/pulley interaction will remain accurate for belt drive systems for which $\Omega < \frac{1}{3}$. The distance harmonic tension waves penetrate into the frictional support is accurately predicted by the quasi-static solution, even for large Ω . For $\Omega > 10$, the frictional support acts effectively as an anechoic termination.

Acknowledgment

The authors gratefully acknowledge the Ford Motor Company for supporting this research endeavor.

References

- Barker, C. R., Oliver, L. R., and Brieg, W. F., 1991, "Dynamic Analysis of Belt Drive Tension Forces During Rapid Engine Acceleration," SAE Congress, Detroit, MI, Paper No. 910687, pp. 239–254.
- Beikmann, R. S., Perkins, N. C., and Ulsoy, A. G., 1996, "Free Vibration of Serpentine Belt Drive Systems," *ASME Journal of Vibration and Acoustics*, Vol. 118, pp. 406–413.
- Euler, M. Leonard, 1762, "Remarques sur l'effect du frottement dans l'equilibre," *Mém. Acad. Sci.*, pp. 265–278.
- Fawcett, J. N., 1981, "Chain and Belt Drives—A Review," *Shock & Vibration Digest*, Vol. 13, No. 5, pp. 5–12.
- Firbank, T. C., 1970, "Mechanics of the Belt Drive," *International Journal of Mechanical Sciences*, Vol. 12, pp. 1053–1063.
- Gerbert, G. G., 1991, "On Flat Belt Slip," *Vehicle Tribology, Tribology Series 16*, Elsevier, Amsterdam, pp. 333–339.
- Gerbert, G. G., 1996, "Belt Slip—A Unified Approach," *ASME Journal of Mechanical Design*, Vol. 118, pp. 432–438.
- Givoli, D., 1991, "Review Article: Non-reflecting Boundary Conditions," *Journal of Computational Physics*, Vol. 94, pp. 1–29.
- Grashof, B. G., 1883, *Theoretische Maschinenlehre*, Bd 2, Leopold Voss, Hamburg.
- Hwang, S.-J., Perkins, N. C., Ulsoy, A. G., and Meckstroth, R. J., 1994, "Rotational Response and Slip Prediction of Serpentine Belt Drive Systems," *ASME Journal of Vibration and Acoustics*, Vol. 116, pp. 71–78.
- Ibrahim, R. A., 1994a, "Friction-Induced Vibration, Chatter, Squeal, and Chaos: Part I—Mechanics of Contact and Friction," *ASME Applied Mechanics Reviews*, Vol. 47, pp. 209–226.
- Ibrahim, R. A., 1994b, "Friction-Induced Vibration, Chatter, Squeal, and Chaos: Part II—Dynamics and Modeling," *ASME Applied Mechanics Reviews*, Vol. 47, pp. 227–253.
- Johnson, K. L., 1985, *Contact Mechanics*, Cambridge University Press, London, Chapter 8.
- Kraver, T. C., Fan, G. W., and Shah, J. J., 1996, "Complex Modal Analysis of a Flat Belt Pulley System With Belt Damping and Coulomb-Damped Tensioner," *ASME Journal of Mechanical Design*, Vol. 118, pp. 306–311.
- Leamy, M. J., and Perkins, N. C., 1998, "Nonlinear Periodic Response of Engine Accessory Drives With Dry Friction Tensioners," *ASME Journal of Vibration and Acoustics*, Vol. 120, pp. 909–916.
- Nikitin, L. V., and Tyurekhodgaev, A. N., 1990, "Wave Propagation and Vibration of Elastic Rods with Interfacial Frictional Slip," *Wave Motion*, Vol. 12, pp. 513–526.
- Oden, J. T., and Martins, J. A. C., 1985, "Models and Computational Methods For Dynamic Friction Phenomena," *Computer Methods in Applied Mechanics and Engineering*, Vol. 52, pp. 527–634.
- Pierre, C., Ferri, A. A., and Dowell, E. H., 1985, "Multi-Harmonic Analysis of Dry Friction Damped Systems Using an Incremental Harmonic Balance Method," *ASME JOURNAL OF APPLIED MECHANICS*, Vol. 52, pp. 958–964.
- Popp, K., and Stelter, P., 1990, "Stick-Slip Vibrations and Chaos," *Philosophical Transactions of the Royal Society of London*, Vol. A332, pp. 89–105.
- Smith, E. A. L., 1960, "Pile-Driving Analysis by the Wave Equation," *ASCE Journal of the Soil Mechanics and Foundations Division*, Vol. 86, No. EM 4, Aug., pp. 35–61.
- Smith, I. M., and To, P., 1988, "Numerical Studies of Vibratory Pile Driving," *International Journal for Numerical and Analytical Methods in Geomechanics*, Vol. 12, pp. 513–531.
- Tabor, D., 1981, "Friction—The Present State of Our Understanding," *ASME Journal of Lubrication Technology*, Vol. 103, pp. 169–179.
- Townsend, W. T., and Salisbury, J. K., 1988, "The Efficiency Limit of Belt and Cable Drives," *ASME Journal of Mechanisms, Transmissions, and Automation in Design*, Vol. 110, pp. 303–307.